Journal of Metals, Materials and Minerals, 36(3), e2642, 2026

Hybrid interface effect of g-C_3N_4/ZnO nanocomposites on the photoelectrochemical cathodic protection of 304 stainless steel in chloride solution

Htet Yadanar SOE[1], Thanate NA WICHEAN[2], Julapar SUNTTIPRAPAR[2], Parichart CHAUM[2], Gasidit PANOMSUWAN[1], Oratai JONGPRATEEP[1], and Ratchatee TECHAPIESANCHAROENKIJ[1,*]

[1] *Special Research Unit for Biomass Conversion Technology for Energy and Environment, Department of Materials Engineering, Faculty of Engineering, Kasetsart University, 50 Ngam Wong Wan Rd, Latyao, Chatuchak, 10900, Bangkok*

[2] *Materials Innovation Center, Faculty of Engineering, Kasetsart University, 50 Ngam Wong Wan Rd, Latyao, Chatuchak, 10900, Bangkok*

***Corresponding author e-mail**: fengrct@ku.ac.th

Received date:
3 February 2026
Revised date:
14 May 2026
Accepted date:
21 May 2026

Keywords:
Metal corrosion;
Photoelectrochemical cathodic protection;
g-C_3N_4;
ZnO;
Composite materials

Abstract

The development of efficient and environmentally friendly corrosion protection systems for metals in aggressive environments has become a critical area of research, particularly for stainless steel used in marine and industrial applications. In this study, a series of graphitic carbon nitride (g-C_3N_4) and zinc oxide (ZnO) composites with varying g-C_3N_4 weight ratios (10 wt% and 30 wt%), are integrated to form heterojunction structures with enhanced charge separation and interfacial activity. The g-C_3N_4/ZnO (ZCN) composite thin films were prepared using a facile thermal mixing method and were characterized using XRD, SEM, BET, FTIR, UV-Vis, and PL to confirm their structural, morphological, and optical properties. Electrochemical impedance spectroscopy (EIS) and potentiodynamic polarization measurements of the ZCN thin films and 304 stainless steel samples under 3.5 wt% NaCl solution showed higher photocurrent density, more negative photopotential displacement, and lower charge-transfer resistance, confirming accelerated electron migration from the ZCN thin film to the stainless-steel substrate. The open circuit potential (OCP) of the steel shifted negatively under illumination, confirming the generation of photogenerated cathodic protection. These results highlight the critical role of the hybrid interface and optimized g-C_3N_4 content in improving light-driven corrosion protection systems. The 10 wt% g-C_3N_4/ZnO nanocomposite offers a promising approach for the development of efficient photoelectrochemical coatings aimed at protecting stainless steel in harsh electrolyte environments.

1. Introduction

Corrosion in marine environments remains a critical engineering challenge, driven primarily by chloride ions, dissolved oxygen, solar radiation, and biological activity. These factors accelerate electrochemical corrosion, leading to progressive structural degradation and substantial economic costs. Conventional corrosion protection strategies rely on methods such as coatings, chemical inhibitors, and sacrificial cathodic protection. In recent years, photoelectrochemical cathodic protection (PECCP) has emerged as a promising green alternative, as it utilizes solar energy to generate photogenerated electrons from semiconductor materials, thereby shifting the corrosion potential of metals to more negative values and suppressing anodic dissolution. Recent studies have demonstrated the effectiveness of PECCP systems in marine environments, $Zn_3In_2S_6$/$ZnMoO_4$ nanocomposites exhibited significantly enhanced photocurrent densities and achieved over 65% corrosion resistance for carbon steel in simulated seawater [1]. And WO_3/Bi_2WO_6 Z-scheme heterojunctions have been reported to provide synergistic anticorrosion performance under visible-light irradiation by promoting efficient charge separation [2].

In PECCP systems, the overall protection performance is governed by the semiconductor's light absorption capability, charge carrier separation efficiency, and appropriate band alignment with the metal substrate. Zinc oxide (ZnO) is widely recognized as an effective semiconductor material due to its favorable conduction band position, wide band gap (~3.2 eV), minimal toxicity, and natural abundance. Nevertheless, its real-world photoelectrochemical efficiency is constrained by fast electron–hole recombination when exposed to solar light. To address this limitation, strategies such as electrolyte modification [3], morphology control [4], and heterojunction construction [5,6]. ZnO photoanodes coupled with 304 stainless steel can generate strong photoinduced cathodic polarization in saline media, leading to notable negative potential shifts and milliampere-level photocurrents under illumination [7].

Among various strategies, significant research efforts have focused on developing ZnO/graphitic carbon nitride (g-C_3N_4) heterostructured systems. g-C_3N_4 is a metal-free polymeric semiconductor with a band gap of about 2.7 eV, which facilitates enhanced visible-light absorption [8,9]. It also exhibits excellent chemical stability, low cost, and environmental benignity. More importantly, g-C_3N_4 can act as a visible-light photosensitizer when coupled with wide band gap semiconductors like ZnO, forming Z-scheme or type-II heterojunctions

that promote efficient charge separation while extending the spectral response into the visible region [10]. Several studies have highlighted the potential of ZnO/g-C_3N_4 heterojunctions in photocatalysis and photoelectrochemical applications. Bu *et al.* demonstrated that films incorporating g-C_3N_4 can deliver photocathodic protection to 304 stainless steel under visible-light irradiation, where effective photo-induced electron transfer led to pronounced negative shifts in corrosion potential [11]. Zhang *et al.* reported that g-C_3N_4-based coating systems were capable of maintaining long-term cathodic protection for metallic substrates due to enhanced absorption in the visible region [12]. In photoelectrochemical cathodic protection systems, semiconductor heterostructures such as ZnO/g-C_3N_4 are also capable of generating reactive oxygen species (ROS), such as superoxide ($^{\bullet}O_2^-$) and hydroxyl ($^{\bullet}OH$) radicals, when subjected to light exposure [13]. This multifunctional function have the strong potential of these materials to enhance the resistance of stainless steel and other alloys against corrosion in harsh marine environments [10]. However, the synergistic application of ZnO and g-C_3N_4 for corrosion inhibition and it remains challenges. The influence of varying the ZnO/g-C_3N_4 composition ratio on corrosion protection performance remains insufficiently examined. In the previous study, the coupling with ZnO in the dark, the mixed potential shifted negatively to about –0.17 V, while under illumination the ZnO/304 SS system reached a stable OCP of around –0.36 V, corresponding to a potential drop of 0.19 V. Among the C_3N_4@ZnO composites, the 1 wt% C_3N_4@ZnO sample exhibited the most pronounced cathodic polarization, achieving a stable photoinduced OCP of approximately –0.40 V with a maximum potential drop of 0.21 V. With further increases in C_3N_4 content, the photoinduced OCP became less negative, reaching about –0.35 V, –0.36 V, and –0.32 V for the 2 wt%, 3 wt%, and 5 wt% composites, respectively. These results indicate that a low C_3N_4 loading is more effective in promoting photoinduced cathodic polarization [9].

In this work, the photoelectrochemical cathodic protection performance of ZnO composites containing 10 wt% and 30 wt% g-C_3N_4 was systematically investigated. ZnO composites containing varying amounts of g-C_3N_4 were analyzed to investigate their optical performance, charge-transfer behavior, and resistance to structural degradation. By coupling g-C_3N_4, which responds effectively to visible light, with the ultraviolet-active ZnO phase, the composites achieved enhanced solar energy harvesting efficiency. The materials produced were systematically analyzed to determine their structural attributes, optical properties, and electrochemical efficiency. This research work showed to develop green, effective coatings for corrosion inhibition in harsh marine environments.

2. Experimental

2.1 Materials

Zinc oxide (ZnO) and ITO were procured from KOSDAQ (Republic of Korea) and, Kaivo Co., Ltd. respectively. Industrial grade 304 stainless steel (304SS) were used. Melamine (purity 99%), Nafion solution, and organic solvents such as methanol, acetone, and ethanol, were purchased from Sigma Co., Ltd. (Germany). All experimental operations were conducted using deionized water. g-C_3N_4 was synthesized via thermal condensation of melamine [14].

2.2 Preparation of g-C_3N_4/ZnO (ZCN) Composites

ZnO/g-C_3N_4 nanocomposites with predetermined mass ratios were fabricated by dispersing pre-synthesized g-C_3N_4 powders (0.1 g for 10 wt% loading and 0.3 g for 30 wt% loading, relative to a fixed ZnO content of 1.0 g) into 80 mL of methanol containing 1.0 g of ZnO. The resulting suspensions were heated at 80°C under constant stirring until the solvent was fully removed. The dried composite precursors were transferred to semi-closed ceramic crucibles and calcined in air at 500°C for 2 h with a heating rate of 5°C·min^{-1}. following natural cooling, the resulting materials were mechanically ground to produce uniform fine powders. These composites were produced and defined as ZCN-1 and ZCN-3, corresponding to g-C_3N_4 loadings of 10 wt% and 30 wt%, respectively.

2.3 Fabrication of the ZCN-coated ITO electrodes

ITO glass substrates were successively cleaned by ultrasonic treatment successively in acetone, ethanol and DI water for 5 min per step and then dried. To prepare the coating mixture, 20 mg of the ZCN composite was dispersed in ethanol (1.0 mL), and 10 µL of 5 wt% Nafion was subsequently added to act as a binder. The prepared suspension (40 µL) was drop-cast onto the conductive side of the pre-treated ITO substrates and dried at 60°C for 12 h. Electrical connections were established using high-purity copper wire secured with conductive copper tape, leaving only the coated region exposed as the active area. The thin-film electrode fabrication process is illustrated in Figure 1 below.

2.4 Characterization

The crystalline phases of the samples were characterized through X-ray diffractometer (XRD, Empyrean, Malvern Panalytical). Chemical structure and functional group information were obtained from Fourier-transform infrared spectra collected on a Bruker Alpha-E instrument. The morphological features and microstructural arrangement of the materials were observed by scanning electron microscopy with a Hitachi SU3500 microscope. Nitrogen adsorption–desorption experiments were performed on a 3Flex analyzer to evaluate the specific surface area. The optical behavior of the composites was assessed through UV-visible absorption measurements using a Shimadzu UV-1900 spectrophotometer in the 250 nm to 800 nm region, and steady-state photoluminescence emission spectra were recorded with a HORIBA FluoroMax-Plus system. Potentiodynamic polarization tests were conducted on 304 stainless steel electrodes using an Autolab PGSTAT302N potentiostat in a 3.5 wt% NaCl solution to replicate practical service environments.

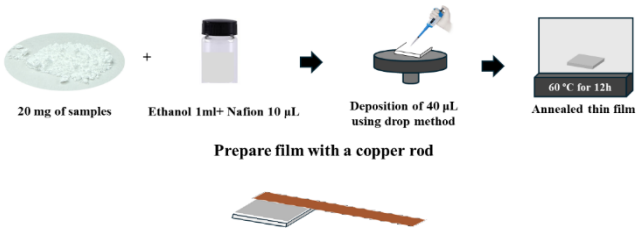

Figure 1. Illustration of the thin-film ZCN-ITO electrode fabrication process.

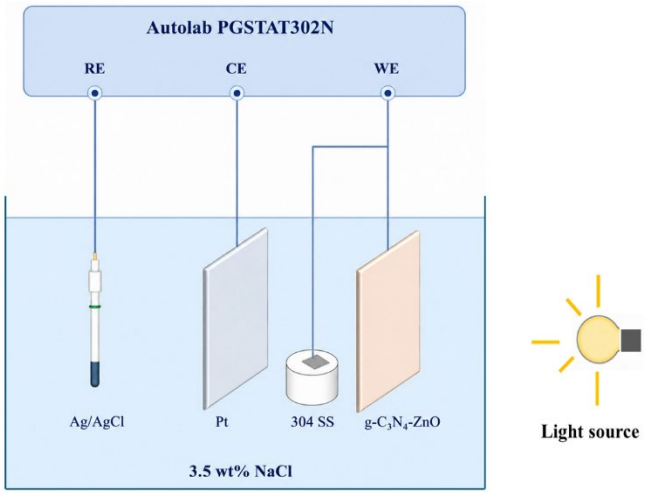

Figure 2. Illustrating the corrosion cell with corrosive electrolyte and the photoelectrode cell.

2.5 Electrochemical Measurements

The corrosion protection performance and photocathodic electron response were assessed employing a standard three-electrode electrochemical configuration coupled to an Autolab PGSTAT302N workstation, as shown in Figure 2. ZCN-coated ITO glass and 304 stainless steel substrates were employed as the working electrodes. A platinum mesh was used as the counter electrode to complete the electrochemical system, An Ag/AgCl electrode immersed in saturated KCl was utilized as the reference electrode to provide a stable and reproducible potential. A 3.5 wt% NaCl aqueous solution was used as the electrolyte to mimic chloride-rich marine environments. Electrochemical impedance spectroscopy (EIS) measurements were carried out over a frequency range of 100 kHz to 10 mHz. Variations in open-circuit potential were monitored under simulated solar illumination for photoinduced cathodic protection behavior. The measurements were repeated under the same conditions to ensure reproducibility.

3. Results and Discussion

3.1 X-ray Diffraction (XRD)

The crystalline structures of the prepared composites were analyzed using an Empyrean X-ray diffractometer (XRD). The diffraction peaks, as shown in Figure 3, were observed at 31.7°, 34.5°, 36.3°, 47.6°, 62.8°, 66.4°, and 68.0°, corresponding to the (100), (002), (101), (102), (110), (103), and (200) planes of the hexagonal wurtzite lattice, thereby confirming the formation of phase-pure ZnO in agreement with standard crystallographic database references [15]. For the g-C_3N_4 precursor, characteristic diffraction peaks related to its polymeric layered architecture were observed at 12.9° and 27.3°, corresponding to the (100) attributed to the (100) in-plane structural periodicity and the (002) interlayer stacking reflection of graphitic carbon nitride sheets, respectively. The relatively weak diffraction peak near 12.8° is attributed to the in-plane atomic ordering of g-C_3N_4, arising from its nitrogen-rich porous framework [16]. The XRD patterns of the composites mainly display the characteristic diffraction peaks of ZnO. No distinct diffraction peak corresponding to g-C_3N_4, particularly the typical peak at around 27.3°, is observed in the composites containing 5 wt%, 10 wt% and 15 wt% g-C_3N_4. This may be attributed to the low crystallinity and weak diffraction intensity of g-C_3N_4 in the composite [17]. Therefore, the incorporation of g-C_3N_4 cannot be confirmed based on XRD analysis alone. However, the characteristic vibration bands observed in the FTIR spectra verify the presence of g-C_3N_4 in the composites.

3.2 Fourier-transform infrared (FTIR) spectroscopy

The structural features of the synthesized materials were examined using Fourier-transform infrared (FTIR) spectroscopy, and the corresponding spectra are presented in Figure 4. The FTIR spectrum of g-C_3N_4 exhibits two prominent absorption bands at approximately 1232 cm^{-1} and 1640 cm^{-1}, which are assigned to the stretching vibrations of C-N and C=N bonds, respectively. An additional absorption band located near 810 cm^{-1} is associated with the characteristic breathing

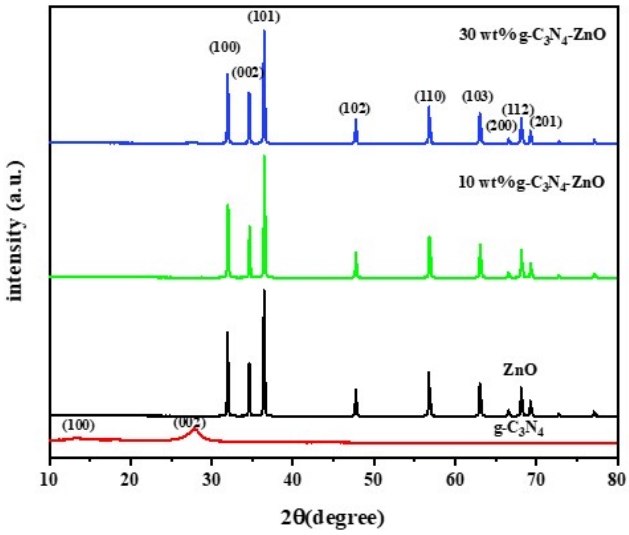

Figure 3. XRD results of pristine ZnO, g-C_3N_4, and ZCN composites.

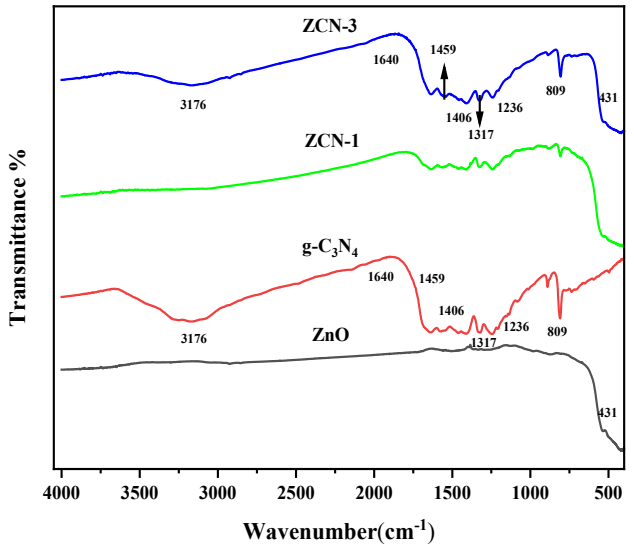

Figure 4. FTIR spectra of ZnO, g-C_3N_4, and ZCN composites.

mode of triazine ring units, which is a well-known fingerprint feature of graphitic carbon nitride [18]. For ZnO, this broad absorption region is typically associated with surface hydroxyl groups and physically adsorbed moisture. The presence of characteristic g-C_3N_4 absorption bands in the FTIR spectra of the ZCN composites confirms the confirmed embedding of g-C_3N_4 throughout the ZnO structure. Moreover, the absorption intensity in the 1232 cm^{-1} to 1640 cm^{-1} region increases progressively with higher g-C_3N_4 loading, suggesting a more significant role of g-C_3N_4 within the composite [19]. These FTIR findings demonstrate that characteristic functional groups of g-C_3N_4 and ZnO are both present, supporting the effective synthesis of the composites.

3.3 Morphological and elemental analysis of ZCN Composites

The surface morphologies of ZCN composites containing different g-C_3N_4 loadings were investigated using scanning electron microscopy (SEM), as presented in Figure 5. At a lower g-C_3N_4 content of ZCN-1, the ZnO particles largely retained their intrinsic structural features, while g-C_3N_4 was only sparsely observed on the ZnO surface [20]. These observations suggest relatively weak interfacial interactions at low g-C_3N_4 loading, with g-C_3N_4 primarily present as thin surface layers or discrete domains on the ZnO particles [21]. When the g-C_3N_4 content was further increased in the ZCN-3 sample, a markedly more homogeneous distribution of g-C_3N_4 was observed. SEM observations show that layered g-C_3N_4 sheets extend through the ZnO particle assembly, indicating intimate interfacial contact that markedly affects the overall morphology and structural features of the composite [22]. An optimal interfacial interaction is required to balance charge separation, transfer, and utilization. In ZCN-3, excessive interaction or higher g-C_3N_4 content may induce increased charge recombination, or reduced the active ZnO sites, thereby limiting photocathodic efficiency [23]. Energy-dispersive X-ray spectroscopy (EDS) analysis (Figure 6) confirms the presence of Zn, O, C, and N elements in the optimized composite containing ZCN-1, with no detectable impurity elements. These observations demonstrate the effective integration of g-C_3N_4 within the ZnO-based composite, confirming both the material's high purity and the consistency of the synthesis procedure.

3.4 Optical Characterization: UV-Vis and PL spectroscopy

The optical characteristics of the synthesized materials were investigated using ultraviolet-visible (UV-Vis) diffuse reflectance spectroscopy, with the corresponding spectra shown in Figure 7(a). The UV-Vis diffuse reflectance spectra reveal that the absorption edges of g-C_3N_4 and ZnO occur at approximately 410 nm and 350 nm, respectively [24]. In comparison with pristine g-C_3N_4 and ZnO, the ZCN composites, most notably ZCN-1, show a clear increase in optical absorption intensity and extended light-harvesting capability. This enhancement is attributed to the effective incorporation of g-C_3N_4 into the ZnO matrix and the formation of interfacial heterostructures [25]. In addition, the ZCN composites exhibit a broadened absorption response over the 280 nm to 800 nm wavelength range, indicating enhanced solar light harvesting capability. This improvement promotes more efficient charge transfer and induces a red shift in the absorption edge, thereby decreasing the effective band gap [26]. The optical band gap energies were determined using the beer lambert, described by the relation

$$(\alpha h\nu)^{n} = A\left(h\nu - E_g\right) \quad (1)$$

where α represents the absorption coefficient, h is Planck's constant, ν is the photon frequency, A is a proportionality constant, E_g denotes the band gap energy, n indicates the electronic transition type, with n = 1/2 for direct and n = 2 for indirect transitions, ZnO is direct band-gap, whereas g-C_3N_4 is indirect [27,28].

Based on this analysis, the band gap energies of g-C_3N_4, ZnO, ZCN-1 and ZCN-3 were estimated to be approximately 2.65 eV, 3.25 eV, 2.89 eV, and 2.95 eV, respectively, as illustrated in Figure 7(b). Notably, the ZCN-1 composite exhibits an intermediate band gap, and its improved suitability for visible-light-driven.

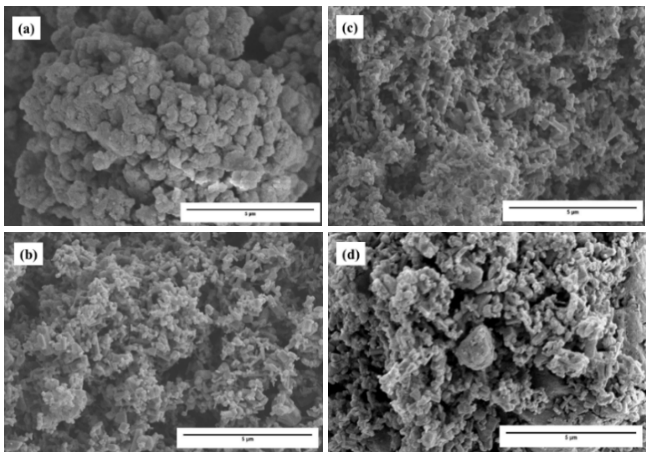

Figure 5. SEM results of (a) g-C_3N_4, (b) ZnO, (c) ZCN-1 and (d) ZCN-3 composites.

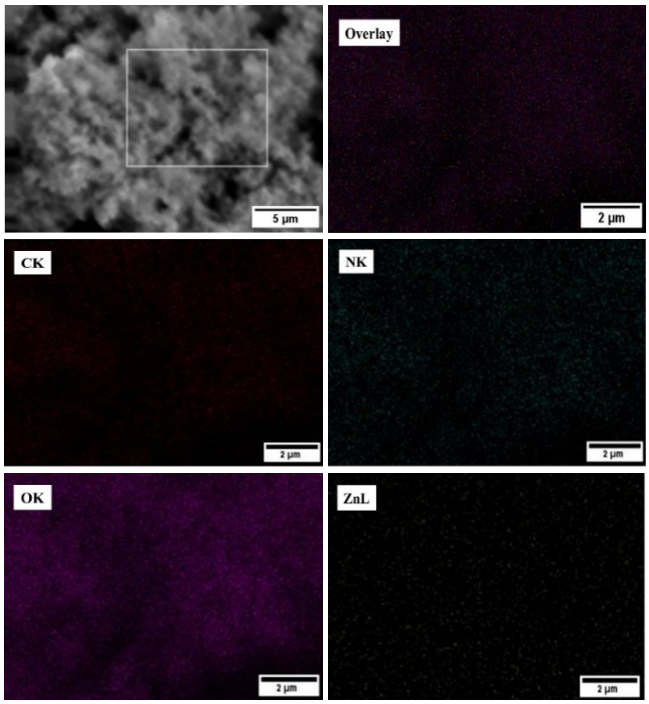

Figure 6. EDS elemental analysis of the ZCN-1 composite.

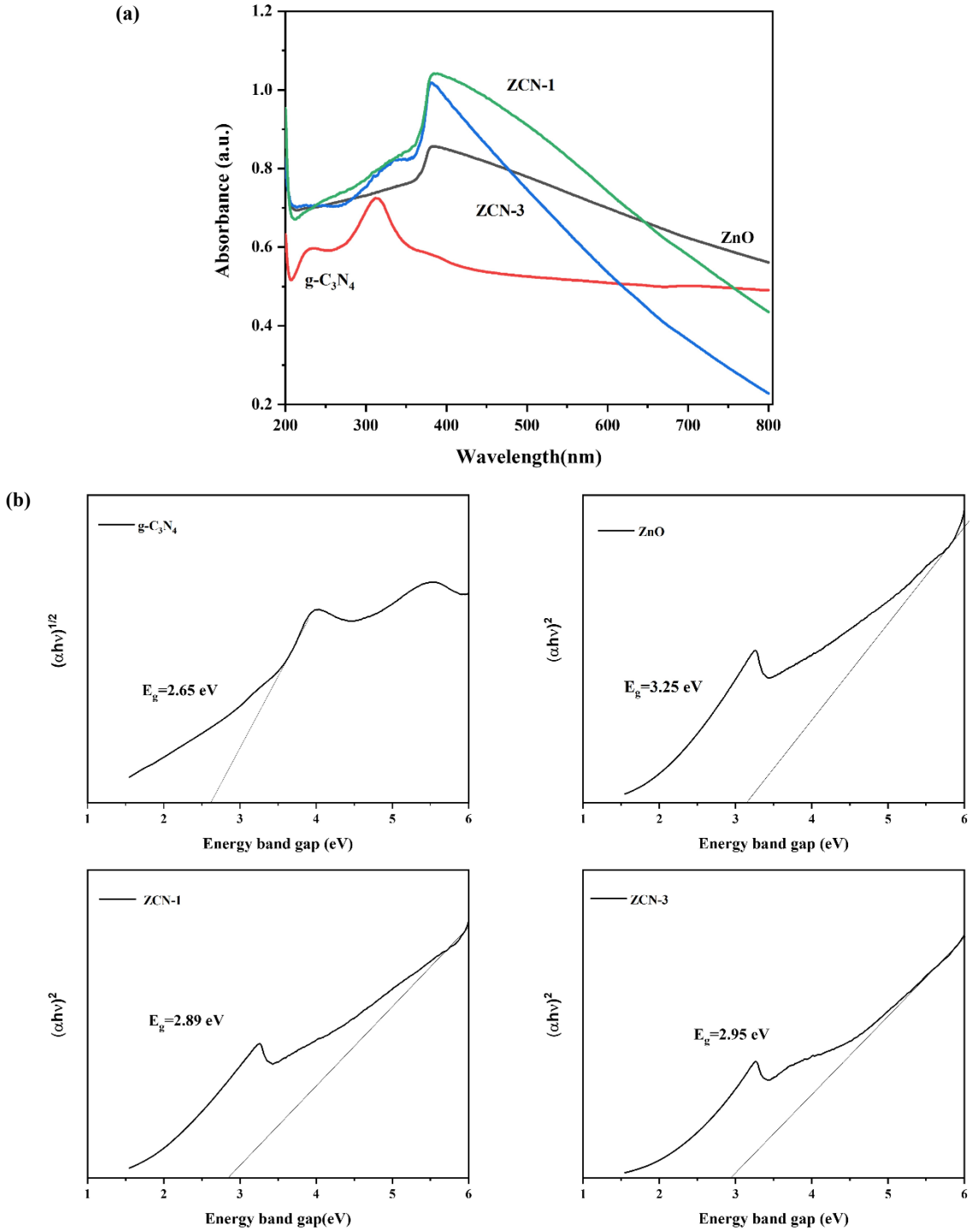

Figure 7. (a) UV-Vis spectra, and (b) corresponding optical band gap plots of pristine ZnO, g-C_3N_4, and ZCN composites.

3.5 Photoluminescence (PL) analysis

The photogenerated electron-hole (e-h) pair separation of the samples was assessed by photoluminescence (PL) spectroscopy. In semiconductor materials, PL emission mainly arises from the radiative recombination of photoexcited charge carriers [29]. As illustrated in Figure 8, pristine g-C_3N_4 displays a broad emission peak centered at around 461 nm, corresponding to band-to-band recombination processes. In comparison, the ZCN-1 composite displays a significantly decrease in PL intensity relative to g-C_3N_4 and a slightly lower intensity than that of pure ZnO and ZCN-3 composite. This decrease in emission intensity indicates a suppression of electron–hole recombination and consequently enhance photo-induced charge transfer efficiency.

3.6 Photocathodic protection performance

3.6.1 Photocurrent density

The photocathodic protection behavior of ZnO, g-C_3N_4, ZCN-1, and ZCN-3 composites was examined using transient photocurrent

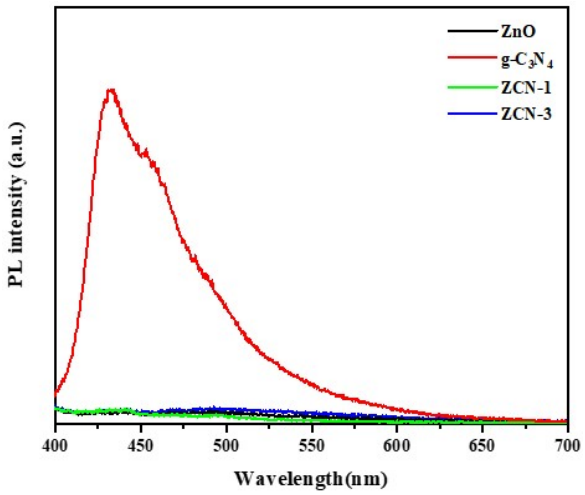

Figure 8. Photoluminescence spectra of ZnO, g-C_3N_4, ZCN-1 and ZCN-3 composite.

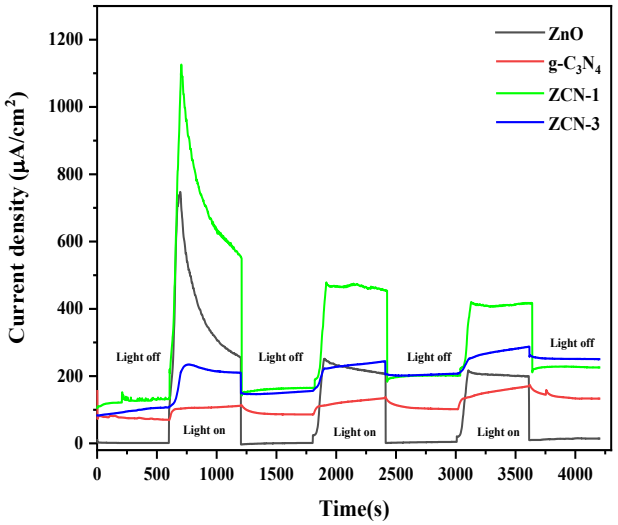

Figure 9. Transient photocurrent responses of ZnO, g-C_3N_4, ZCN-1, and ZCN-3 composites measured under alternating visible-light illumination and dark conditions.

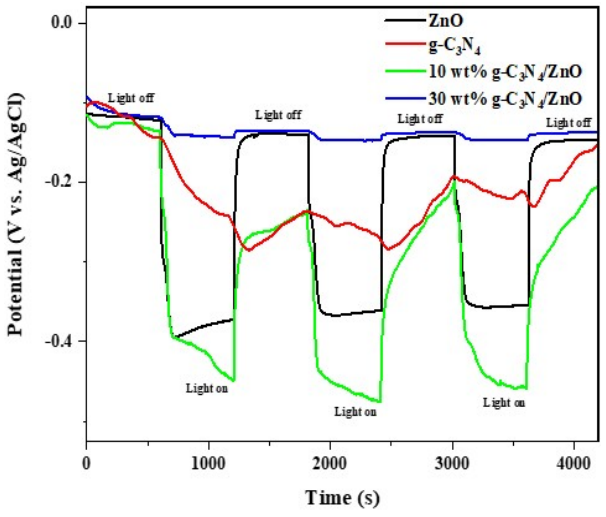

Figure 10. Open-circuit potential (OCP) responses of ZnO, g-C_3N_4, ZCN-1, and ZCN-3 composites under alternating visible-light illumination.

density measurements under intermittent visible-light illumination with 600 s on/off cycles. This method is widely used to evaluate the efficiency of photo-induced electron transport from photoactive materials to a coupled metal substrate, thereby reflecting the corrosion-protection capability of the system. As shown in Figure 9, an increase in photocurrent density is observed upon light irradiation, indicating efficient migration of photogenerated electrons from the photoanode to the 304 stainless-steel substrate.

The rapid and reproducible photo response confirms the effective generation and transfer of charge carriers under visible-light excitation. Furthermore, the positive direction of the recorded photocurrent verifies the n-type semiconducting nature of the synthesized materials, which exhibit photoanode behavior [20]. Among the examined samples, pristine ZnO exhibits a moderate photocurrent density in the range of 200 μA·cm^{-2} to 300 μA·cm^{-2}, whereas pure g-C_3N_4 delivers the lowest response, varying from 100 μA·cm^{-2} to 180 μA·cm^{-2}. The formation of ZnO/g-C_3N_4 heterostructures significantly enhances photocurrent generation, with ZCN-1 achieving the highest values of approximately 500 μA·cm^{-2} to 600 μA·cm^{-2}. By contrast, ZCN-3 presents a lower photocurrent density (220 μA·cm^{-2} to 300 μA·cm^{-2}), which can be attributed to excessive g-C_3N_4 content that limits light harvesting and restricts interfacial charge transfer. interfacial charge transport. The improvement in photocurrent performance for the ZCN-1 composite is primarily attributed to the formation of an optimized g-C_3N_4/ZnO heterojunction.

This heterostructure effectively suppresses the recombination of photogenerated electron–hole pairs and promotes interfacial charge transfer, thereby enhancing photo-induced electron transport and photocathodic protection efficiency This behavior is consistent with previously reported S-scheme ZCN heterostructures, in which favorable band alignment promotes efficient charge-carrier transport and enhances overall photocathodic protection efficiency [25,26]. ZCN-1 exhibits the most favorable performance due to the formation of an effective heterointerface that promotes electron transfers to the metal, enhancing corrosion protection [11].

3.6.2 Open circuit potential (OCP)

The photocathodic protection performance of the prepared composites was further evaluated with the open-circuit potential (OCP) of 304 stainless-steel electrodes under intermittent visible-light illumination, as shown in Figure 10. Upon coupling the stainless-steel substrate with the photoanodic materials, a pronounced negative shift in OCP is observed, ranging from approximately –0.10 V to –0.45 V, depending on the composite composition.

This negative displacement is associated with the more negative Fermi level of the photoanodes under illumination, which enables efficient injection of photogenerated electrons into the metal substrate and thereby suppresses anodic corrosion reactions on the metal. The open-circuit potential (OCP) responses of stainless-steel electrodes coupled with different photoelectrodes reveal distinct degrees of cathodic polarization under visible-light illumination, highlighting the influence of composite composition on photoelectrochemical protection performance [30]. Among all samples, the ZCN-1 coupled stainless-steel electrode exhibits the most negative potential shift, reaching approximately −0.45 V, indicating the strongest cathodic

protection effect. In comparison, stainless steel coupled with ZnO, g-C_3N_4, and ZCN-3 shows less negative OCP values of about –0.35 V, –0.28 V, and –0.13 V, respectively [22]. The ZCN-1 electrode exhibited the largest negative potential shift (–0.45 V), which is slightly more negative than the previously reported 1 wt% C_3N_4@ZnO system (–0.40 V), indicating improved cathodic polarization and electron transfer efficiency [9]. The superior performance of ZCN-1 can be attributed to the formation of an optimized ZnO/g-C_3N_4 heterojunction, which promotes efficient photogenerated charge separation and electron transfer to the stainless-steel surface, thereby stabilizing the cathodic protection potential and enhancing corrosion resistance.

With a low content of g-C_3N_4, photogenerated electrons from ZnO can be transferred through the composite to the 304 stainless steel surfaces, producing a distinct negative shift in OCP that reflects effective cathodic protection. In contrast, higher C_3N_4 content increasingly masks the ZnO surface, impeding electron transport to the metal substrate and thereby reducing the OCP shift and photocathodic anticorrosion efficiency. Furthermore, the negative OCP observed for g-C_3N_4 under dark conditions indicates a charge storage behavior due to the slow release of stored electrons.

As illustrated in Figure 10, the open-circuit potential (OCP) of the working electrode rapidly moved toward more negative values upon visible-light exposure, indicating the successful injection of photogenerated electrons from the photoelectrode into the 304 stainless-steel substrate [11]. This cathodic shift confirms that the stainless-steel surface was maintained under effective photocathodic protection conditions during illumination.

3.6.3 Electrochemical impedance spectroscopy (EIS)

Electrochemical impedance spectroscopy (EIS) measurements were carried out to further evaluate the corrosion protection performance of different photoelectrodes under light irradiation. The corresponding Nyquist plots obtained for the working electrodes under illumination are presented as shown in Figure 11. Based on the equivalent circuit model, R_s represents the solution resistance, C_{dl} denotes the double-layer capacitance, Z_w corresponds to the mass transfer (Warburg) impedance, and R_{ct} is the charge-transfer resistance [31].

Among the investigated photoelectrodes, the ZCN-1 composite demonstrated the lowest charge transfer resistance (R_{ct}) under both dark and illuminated conditions as summarized in Table 1. In the dark, its R_{ct} value (1098 Ω) was lower than those of ZCN-3 (1615 Ω), pure ZnO (4132 Ω), and g-C_3N_4 (1874 Ω). Upon light irradiation, the R_{ct} of the ZCN-1 composite further decreased to 45 Ω, outperforming ZCN-3 (148 Ω), pure ZnO (92 Ω), and g-C_3N_4 (150 Ω). This significant reduction in charge transfer resistance indicates enhanced photogenerated electron separation and superior electrical conductivity in the ZCN-1 composite under illumination.

The simultaneously lower R_{ct} values observed for the ZCN-1 composite confirm more efficient interfacial charge transport electrons to the 304 stainless steel surfaces. Consequently, this enhanced electron transfer accelerates cathodic reactions and significantly improves the overall photoelectrochemical corrosion protection performance. ZCN-1 exhibited the highest photocurrent density (500 μA·cm^{-2} to 600 μA·cm^{-2}) and the lowest charge-transfer resistance (45 Ω), suggesting efficient generation, separation, and transport of photo-generated charge carriers, which is consistent with previous reports on ZnO/g-C_3N_4 heterojunctions where strong interfacial coupling promoted charge transfer and reduced electron–hole recombination [9].

The notably reduced R_{ct} values associated with the ZCN-1 composite suggest that a larger fraction of photogenerated electrons is efficiently transferred. This enhanced interfacial charge-transfer behavior accelerates photocatalytic cathodic reactions and substantially improves the overall photoelectrochemical corrosion protection performance [32].

Table 1. Charge-transfer resistances (R_{ct}) of different photoelectrodes under dark and light conditions.

Sample	R_{ct} [Ω] (Dark)	R_{ct} [Ω] (Light on)
ZnO	4132	92
g-C_3N_4	1874	150
ZCN-1	1098	45
ZCN-3	1615	148

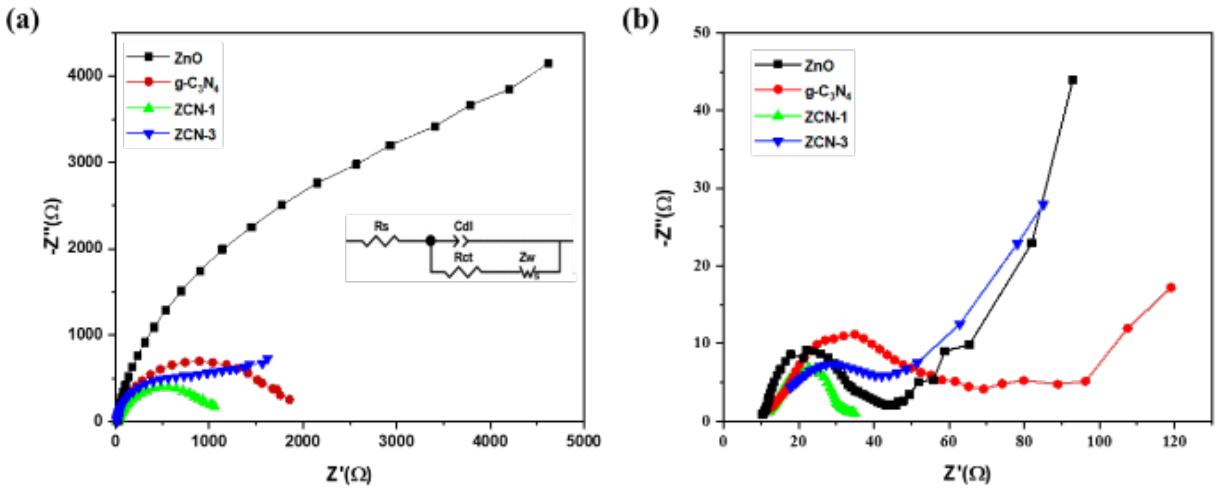

Figure 11. Nyquist plots obtained from electrochemical impedance spectroscopy (EIS) measurements for ZnO, g-C_3N_4, ZCN-1, and ZCN-3 composites recorded under (a) dark conditions, and (b) visible-light irradiation.

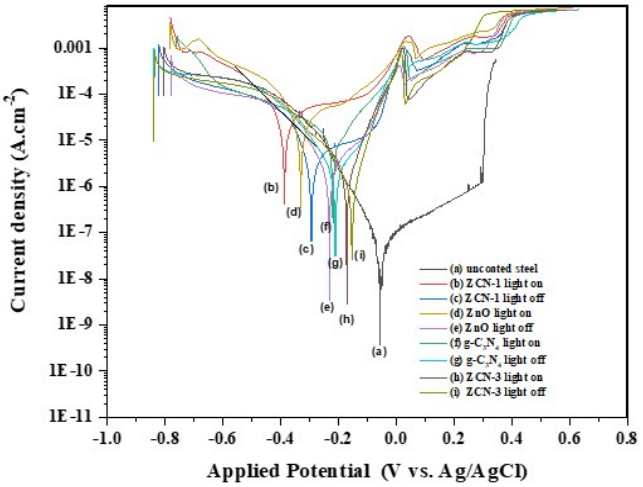

Figure 12. Tafel polarization curves of ZnO, g-C_3N_4, ZCN-1, and ZCN-3 composites measured under light-on and light-off conditions.

3.6.4 Linear polarization

The corrosion potential (E_{corr}) and corrosion current density (i_{corr}) values derived from Tafel polarization measurements are summarized in Table 2. As shown in Figure 12, under visible-light illumination, 304 stainless steel coupled with the ZCN-1 photoanode exhibits the most pronounced cathodic shift, with an E_{corr} of approximately –0.39 V vs Ag/AgCl, indicating the highest photocathodic protection efficiency. In comparison, the E_{corr} values for ZnO, g-C_3N_4, and ZCN-3 photoanodes under illumination are less negative, at approximately –0.32 V, –0.23 V, and –0.19 V vs Ag/AgCl, respectively. In the absence of illumination, all systems show positive shifts in corrosion potential, confirming the essential role of photoexcitation in driving electron transfer.

As summarized in Table 2, visible-light irradiation induces a cathodic displacement of the corrosion potential for all photoanode-coupled systems, verifying the injection of photogenerated electrons into the stainless-steel substrate. Compared to ZCN-3 and g-C_3N_4 photoanodes, the ZnO and ZCN-1 exhibit a significantly enhanced cathodic shift under illumination, demonstrating effective photo-induced electron transfer enabled by the ZnO/g-C_3N_4 heterojunction. ZCN-1 shows the largest potential shift (from –0.29 V to –0.39 V vs Ag/AgCl) under visible light. The current density increases under illumination due to photoelectrochemical activation of photo-generated electron-hole pairs. These photogenerated carriers promote charge transfer at the electrode and electrolyte interface, leading to a higher measured current density. Thus, the increase in current density is mainly related to light-driven electrochemical activity, rather than being a direct indication of accelerated corrosion [33].

The substantial cathodic polarization dominates the protection behavior, resulting in superior photocathodic protection performance. These results are consistent with photocurrent response, open-circuit potential, and electrochemical impedance spectroscopy analyses, confirming that optimized heterojunction formation in ZCN-1 facilitates efficient charge separation and directional electron transport.

3.6.5 Optical microscope

Figure 13 shows the stainless-steel conditions after the polarization test to demonstrate how ZnO, g-C_3N_4 and ZCN photoanodes protect the steel under UV light. As seen in Figure 13(a), the untreated 304 stainless steel surface prior to testing was smooth and free from visible defects. In exposure to the 3.5 wt% sodium chloride solution, severe surface degradation was observed due to aggressive chloride ion (Cl^-) attack, leading to the formation of large corrosion pits, as illustrated in Figure 13(b,d,f,h). When the samples were evaluated under dark conditions, stainless steel coupled with ZnO (Figure 13(b)), g-C_3N_4 (Figure 13(d)), ZCN-1 (Figure 13(f)), and ZCN-3 (Figure 13(h)) all exhibited noticeable pitting corrosion, indicating that effective photo-cathodic protection was not achieved in the absence of light irradiation.

In contrast, under UV illumination, the samples coupled with ZnO (Figure 13(c)), g-C_3N_4 (Figure 13(e)), ZCN-1 (Figure 13(g)), and ZCN-3 (Figure 13(i)) displayed significantly reduced surface damage, with fewer and smaller corrosion pits compared to those tested in the dark. Among these, the stainless-steel sample protected by the

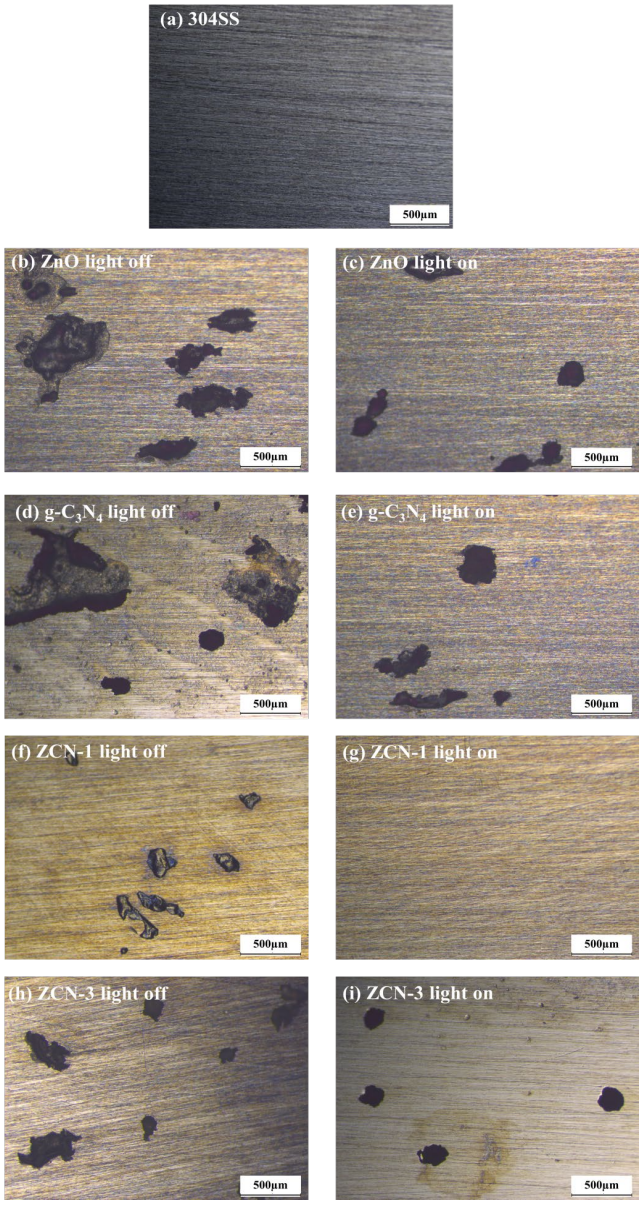

Figure 13. Optical images showing the surface morphology of (a) 304 stainless steel (304 SS) before polarization testing, (b) ZnO, (d) g-C_3N_4, (f) ZCN-1, and (h) ZCN-3 composites light off and (c) ZnO, (e) g-C_3N_4, (g) ZCN-1, and (i) ZCN-3 composites light on conditions after polarization testing.

ZCN-1 photoanode demonstrated the most effective corrosion resistance, showing very small pitting (in micron size) after the test, indicative of strong photocathodic protection. Overall, these macroscopic observations confirm that ZnO, g-C_3N_4, and ZCN photoanodes are capable of protecting 304 stainless steels from corrosion in a 3.5 wt% NaCl environment under UV illumination. Compared with pure ZnO, the ZCN composites exhibit markedly better performance, which can be attributed to the effective role of g-C_3N_4 in enhancing photocathodic protection.

3.7 Surface area and pore size distribution

The enhanced photocathodic protection performance of ZCN-1 can be attributed its specific surface area and pore characteristics as revealed by BET analysis. Figure 14(a) presents the nitrogen adsorption-desorption isotherms of pristine ZnO, g-C_3N_4, and ZCN-1 composite samples measured at 77.3 K over a relative pressure (P/P_0) range of 0.01 to 0.95. All samples display type IV adsorption isotherms accompanied by H3-type hysteresis loops, which are characteristic of mesoporous materials. The hysteresis loops observed within the P/P_0 range of 0.6 to 0.9 are associated with slit-shaped pore structures, typically arising from the aggregation of plate-like particles [34]. The calculated BET surface areas of ZnO, g-C_3N_4, and the ZCN-1 composite are 7 $m^2 \cdot g^{-1}$, 62 $m^2 \cdot g^{-1}$, and 12 $m^2 \cdot g^{-1}$, respectively in Table 3. The increased surface area of the composite relative to pristine ZnO highlights between ZnO and g-C_3N_4, resulting in a higher number of accessible active sites. Figure 14(b) presents the adsorption isotherms, which reveal that the ZCN-1 composite contains pores with average diameters predominantly distributed in the 0 nm to 20 nm range, confirming its mesoporous structure. Such pore architectures are beneficial for enhancing photocatalytic and photoelectrochemical performance by facilitating efficient mass transport and increasing surface reactivity [35].

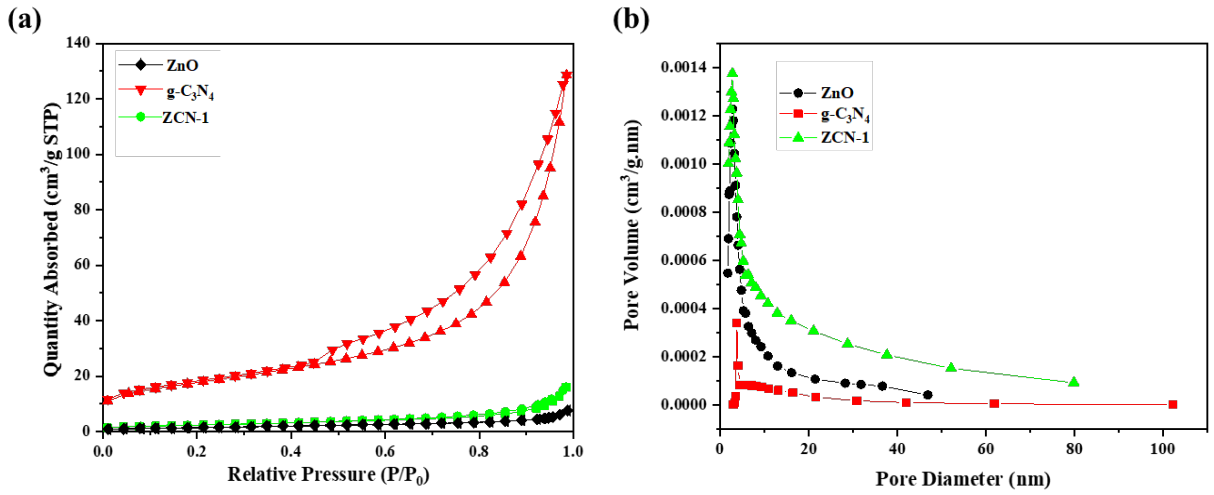

Figure 14. (a) Nitrogen adsorption–desorption isotherms and (b) pore size distribution profiles of ZnO, g-C_3N_4, and ZCN-1 composites.

Table 2. Corrosion potentials (E_{corr}) and corrosion current densities (i_{corr}) obtained from Tafel polarization analysis under dark and visible-light conditions.

Sample	Sample condition	E_{corr} [V vs. Ag/AgCl]	i_{corr} [A·cm^{-2}]
Stainless Steel 304	Uncoated base 304 SS	–0.12	$(1.0 \pm 0.21) \times 10^{-7}$
ZnO	ZnO light on	–0.32	$(2.0 \pm 0.12) \times 10^{-5}$
	ZnO light off	–0.24	$(3.9 \pm 0.31) \times 10^{-6}$
g-C_3N_4	g-C_3N_4 light on	–0.23	$(1.1 \pm 0.47) \times 10^{-5}$
	g-C_3N_4 light off	–0.21	$(4.8 \pm 0.92) \times 10^{-6}$
ZCN-1	ZCN-1 light on	–0.39	$(2.2 \pm 0.68) \times 10^{-5}$
	ZCN-1 light off	–0.29	$(3.5 \pm 1.01) \times 10^{-6}$
ZCN-3	ZCN-3 light on	–0.19	$(1.1 \pm 0.58) \times 10^{-5}$
	ZCN-3 light off	–0.17	$(2.2 \pm 0.37) \times 10^{-6}$

Table 3. BET surface area, total pore volume, and average pore radius of ZnO, g-C_3N_4, and ZCN-1 composites at different g-C_3N_4 loadings.

Samples	Surface area ($m^2 \cdot g^{-1}$)	Total pore volume [$cm^3 \cdot g^{-1}$]	Average pore radius [nm]
ZnO	7	0.012	8.4
g-C_3N_4	62	0.14	0.9
ZCN-1	12	0.025	10.8

4. Conclusion

In this work, 10wt% g-C_3N_4/ZnO (ZCN-1) and 30 wt% g-C_3N_4/ZnO (ZCN-3) composite photoanodes were successfully synthesized and systematically evaluated for their ability to provide light-driven cathodic protection to 304 stainless steel in chloride-rich aqueous environments. Structural and morphological analyses confirmed the formation of well-integrated heterojunction interfaces, g-C_3N_4 embedded in the ZnO particles, enhancing their surface accessibility and mesoporous characteristics. Optical characterization and PL quenching demonstrated that the hybrid interfaces effectively suppress electron–hole recombination and promote more efficient charge separation under illumination. The transient photocurrent response, open-circuit potential shift, EIS fitting, and polarization behavior revealed that the ZCN-1 composite provides the most favorable electronic coupling between the two semiconductors. This optimized composition achieved the highest photocurrent density, largest negative photopotential displacement, and lowest charge-transfer resistance, confirming accelerated electron migration from the composite film to the stainless-steel substrate. The optical microscopy confirmed reduced pit formation, indicating effective mitigation of localized corrosion during light exposure. Overall, the results show that constructing a balanced hybrid heterojunction between ZnO and g-C_3N_4 significantly improves light-responsive electron transfer and enhances photocathodic corrosion protection efficiency. The ZCN-1 composite is identified as the optimal configuration, providing a stable, non-sacrificial, and environmentally sustainable strategy for protecting stainless-steel components in harsh chloride environments. The results demonstrate that semiconductor heterostructures incorporating g-C_3N_4 show strong promise for application in photoelectrochemical corrosion-protection coatings.

Acknowledgements

This research was supported by the Faculty of Engineering, Kasetsart University for the international Ph.D. scholarship. HYS and RT thank the AUN/SEED-Net, JICA for financial support. Kasetsart University Research and Development Institute is acknowledged for the support of the Special Research Unit for Biomass Conversion Technology for Energy and Environment.

References

[1] Z. Jin, Z. Gao, H. Jiang, X. Li, Y. Chen, and X. Zhang, "Corrosion resistance improvement of carbon steel by novel flower cluster photocathodic protection coating in marine environment," *Journal of Building Engineering*, vol. 112, p. 113652, 2025.

[2] J. Tian, Y. Cheng, Z. Zhang, Z. Zhao, Z. Xu, and J. Li, "Photo-generated carrier-directed modulation of WO_3/Bi_2WO_6 Z-scheme heterojunction for marine anti-corrosion and anti-fouling," *npj Materials Degradation*, vol. 9, no. 1, p. 163, 2025.

[3] P. Wipataphan, W. Sripianem, N. B. Oo, T. Na Wichean, B. Dachbumroong, O. Jongprateep, G. Panomsuwan, N. Pewnim, and R. Techapiesancharoenkij, "Photoelectrochemical cathodic protection of amorphous zinc oxide coating on hot rolled steel SS400 in a 3 wt% NaCl solution and a Na_2S-NaOH solution," *Journal of Metals, Materials and Minerals*, vol. 31, no. 4, pp. 129–142, 2021.

[4] S. Yang, J. Wang, C. Liu, P. Ren, Q. Yang, and G. Zhao, "Morphology control and photocatalytic properties of ZnO sheets grown on an AAO template," *Ceramics International*, vol. 47, no. 6, pp. 8610–8617, 2021.

[5] X. Zhang, G. Chen, W. Li, and D. Wu, "Preparation and photocathodic protection properties of ZnO/TiO_2 heterojunction film under simulated solar light," *Materials*, vol. 12, no. 23, p. 3856, 2019.

[6] S. Veerapong, N.B. Oo, B. Dachbumroong, P. Chaum, T. Na Wichean, O. Jongprateep, N. Pewnim, G. Panomsuwan, and R. Techapiesnacharoenkij, "Investigation of photocathodic corrosion protection of ZnO/ZnS thin film for AISI 304 stainless steel in 3.5 wt% NaCl solution," *Journal of Metals, Materials and Minerals*, vol. 35, no. 1, p. e2105, 2025.

[7] R. Techapiesancharoenkij, W. Sripianem, K. Tongpul, C. Peamjharean, T. Na Wichean, T. Meesak, and P. Eiamchai, "Investigation of the photocathodic protection of a transparent ZnO coating on an AISI type 304 stainless steel in a 3% NaCl solution," *Surface and Coatings Technology*, vol. 320, pp. 97–102, 2017.

[8] F. Nabhan, E. M. Fayyad, M. H. Sliem, F. M. Shurrab, K. Eid, G. Nasrallah, and A. M. Abdullah, "ZnO-doped g-C_3N_4 nanocapsules for enhancing the performance of electroless NiP coating—mechanical, corrosion protection, and antibacterial properties," *ACS Omega*, vol. 8, no. 25, pp. 22361–22381, 2023.

[9] Y. Bu, and Z. Chen, "Highly efficient photoelectrochemical anticorrosion for 304 stainless steel by C_3N_4@ZnO composite with quasi-shell-core structure," *RSC Advances*, vol. 4, pp. 45397–45406, 2014.

[10] Y. Lv, Y. Zheng, H. Zhu, and Y. Wu, "Designing a dual-functional material with barrier anti-corrosion and photocatalytic antifouling properties using g-C_3N_4 nanosheet with ZnO nanoring," *Journal of Materials Science & Technology*, vol. 106, pp. 56–69, 2022.

[11] H. Zheng, Y. Liu, Y. Zhou, D. Zhao, D. Wang, L. Yun, D. Zhang, and L. Zhang, "Improved photocathodic protection performance of g-C_3N_4/rGO/ZnS for 304 stainless steel," *Journal of Physics and Chemistry of Solids*, vol. 148, p. 109672, 2021.

[12] J. Jing, Z. Chen, C. Feng, M. Sun, and J. Hou, "Transforming g-C_3N_4 from amphoteric to n-type semiconductor: The important role of p/n type on photoelectrochemical cathodic protection," *Journal of Alloys and Compounds*, vol. 851, p. 156820, 2021.

[13] D. R. Paul, S. Gautam, P. Panchal, S. P. Nehra, P. Choudhary, and A. Sharma, "ZnO-modified g-C_3N_4: A potential photocatalyst for environmental application," *ACS Omega*, vol. 5, no. 8, pp. 3828–3838, 2020.

[14] C. Li, X. Yang, B. Yang, Y. Yan, and Y. Qian, "Synthesis and characterization of nitrogen-rich graphitic carbon nitride," *Materials Chemistry and Physics*, vol. 103, no. 2, pp. 427–432, 2007.

[15] N. Sabri, M. Nawi, and W. Nawawi, "Porous immobilized C-coated N-doped TiO_2 containing in-situ generated polyenes for enhanced visible light photocatalytic activity," *Optical Materials*, vol. 48, pp. 258–266, 2015.

[16] F. Fina, S. K. Callear, G. M. Carins, and J. T. Irvine, "Structural investigation of graphitic carbon nitride via XRD and neutron diffraction," *Chemistry of Materials*, vol. 27, no. 7, pp. 2612–2618, 2015.

[17] F. Hassan, S. N. Backer, I. W. Almanassra, M. A. Atieh, M. Elbahri, and A. Shanableh, "Solar-matched S-scheme ZnO/g-C_3N_4 for visible light-driven paracetamol degradation," *Scientific Reports*, vol. 14, no. 1, p. 12220, 2024.

[18] M. Ramachandra, S. D. K. R. Pai, J. R. Jaleel, and D. Pinheiro, "Improved photocatalytic activity of g-C_3N_4/ZnO: A potential direct Z-scheme nanocomposite," *Chemistry Select*, vol. 5, no. 38, pp. 11986–11995, 2020.

[19] M. Suhag, A. Khatun, I. Tateishi, M. Furukawa, H. Katsumata, and S. Kaneco, "One-step fabrication of the ZnO/g-C_3N_4 composite for visible light-responsive photocatalytic degradation of bisphenol E in aqueous solution," *ACS Omega*, vol. 8, pp. 11824–11836, 2023.

[20] Q. Sun, Y. Sun, M. Zhou, H. Cheng, H. Chen, B. Dorus, M. Lu, and T. Le, "A 2D/3D g-C_3N_4/ZnO heterojunction enhanced visible-light driven photocatalytic activity for sulfonamides degradation," *Ceramics International*, vol. 48, no. 5, pp. 7283–7290, 2022.

[21] C. Yan, A.M. Abed, M. Shaban, X. Li, X. Zhou, G. Lei, S. Abdullaev, and I. Mahariq, "Superb photocatalytic H_2 production/tetracycline pollutant degradation by synthesizing novel and recyclable ternary g-C_3N_4-based photocatalyst: Characterization, optimization, mechanism, and toxicity assessment," *Journal of Water Process Engineering*, vol. 69, p. 106642, 2025.

[22] H. Asghar, M. Saeed, F. S. Mirsafi, M. K. Ismael, T. Leißner, and Y. K. Mishra, "Zinc oxide–graphitic carbon nitride composites: Synthesis, properties, and application scopes in environmental remediations," *Small*, vol. 21, e09637, 2025.

[23] S. Qiu, and J. Li, "High-efficiency Ag-modified ZnO/g-C_3N_4 photocatalyst with 1D-0D-2D morphology for methylene blue degradation," *Molecules*, vol. 29, no. 10, p. 2182, 2024.

[24] X. Wang, K. Maeda, A. Thomas, K. Takanabe, G. Xin, J. M. Carlsson, K. Domen, and M. Antonietti, "A metal-free polymeric photocatalyst for hydrogen production from water under visible light," *Nature Materials*, vol. 8, no. 1, pp. 76–80, 2009.

[25] J.-X. Sun, Y.-P. Yuan, L.-G. Qiu, X. Jiang, A.-J. Xie, Y.-H. Shen, and J, Zhu, "Fabrication of composite photocatalyst g-C_3N_4–ZnO and enhancement of photocatalytic activity under visible light," *Dalton Transactions*, vol. 41, no. 22, pp. 6756–6763, 2012.

[26] B. Sert, Z. Bilici, K. Ocakoglu, N. Dizge, T. S. Rad, and A. Khataee, "Preparation of S-scheme g-C_3N_4/ZnO heterojunction composite for highly efficient photocatalytic destruction of refractory organic pollutant," *Catalysts*, vol. 13, no. 3, p. 485, 2023.

[27] J. Tauc, "Optical properties and electronic structure of amorphous Ge and Si," *Materials Research Bulletin*, vol. 3, no. 1, pp. 37–46, 1968.

[28] P. Makuła, M. Pacia, and W. Macyk, "How to correctly determine the band gap energy of modified semiconductor photocatalysts based on UV–Vis spectra," *Journal of Physical Chemistry Letters*, vol. 9, pp. 6814–6817, 2018.

[29] X. Zhang, J. Qin, Y. Xue, P. Yu, B. Zhang, L. Wang, and R. Liu, "Effect of aspect ratio and surface defects on the photocatalytic activity of ZnO nanorods," *Scientific Reports*, vol. 4, no. 1, p. 4596, 2014.

[30] H. Xu, W. Liu, L. Cao, G. Su, and R. Duan, "Preparation of porous TiO_2/ZnO composite film and its photocathodic protection properties for 304 stainless steel," *Applied Surface Science*, vol. 301, pp. 508–514, 2014.

[31] A. C. Lazanas, and M. I. Prodromidis, "Electrochemical impedance spectroscopy—A tutorial," *ACS Measurement Science Au*, vol. 3, no. 3, pp. 162–193, 2023.

[32] R. Guan, J. Li, J. Zhang, Z. Zhao, D. Wang, H. Zhai, and D. Sun, "Photocatalytic performance and mechanistic research of ZnO/g-C_3N_4 on degradation of methyl orange," *ACS Omega*, vol. 4, no. 24, pp. 20742–20747, 2019.

[33] Z.-X. Liu, J.-J. Tian, P. Liu, J.-C. Liu, and J.-K. Liu, "Design and synthesis of mosaic ZnO/g-C_3N_4 heterojunction materials with excellent anticorrosion performance," *Industrial & Engineering Chemistry Research,* vol. 63, no. 30, pp. 13218-13229, 2024.

[34] S. Brunauer, P. H. Emmett, and E. Teller, "Adsorption of gases in multimolecular layers," *Journal of the American Chemical Society*, vol. 60, no. 2, pp. 309–319, 1938.

[35] S. Pourali, R. Amrollahi, S. Alamolhoda, and S. Masoudpanah, "In situ synthesis of ZnO/g-C_3N_4 based composites for photodegradation of methylene blue under visible light," *Scientific Reports*, vol. 15, no. 1, p. 462, 2025.